Hierarchically Porous Rutile Titania: Harnessing Spontaneous Compositional Change in Mixed-Metal Oxides

Eric S. Toberer,[†] Jan D. Epping,[‡] Bradley F. Chmelka,*,[‡] and Ram Seshadri*,[†]

Materials Department and Materials Research Laboratory and Department of Chemical Engineering, University of California, Santa Barbara, California 93106

In numerous applications involving fluid flow through a porous structure, performance improvements, such as better flow characteristics and increased fluid−solid contact, are obtained when multiple length scales of porosity are present in the porous medium. To this end, we have developed a route to hierarchically porous rutile titania that obviates the need for preformed or preassembled structure-directing agents. The preparation involves the successive leaching of phases and components from a dense composite of wurtzite ZnO and inverse spinel Zn_2TiO_4. The resulting monoliths are composed of grains of highly crystalline rutile titania and possess a hierarchy of interconnected pores with length scales of 5 μm and 100 nm. Ex situ solid-state ^{67}Zn and ^{47,49}Ti NMR has helped probe local environments around these elements in both the mixed and pure crystalline materials that are formed during the leaching processes.

Introduction

The formation of porous inorganic structures for applications in separations, catalysis, sensing, and power generation has attracted significant attention in recent years. The use of porous materials helps increase contact between solid and fluid phases leading to improved performance. As the different applications invariably require specific pore wall chemistry and morphology, there has been great emphasis placed on the development of new preparative routes to porous materials. Numerous structure-directing agents have been employed with great success for templating the growth of porous materials. Latex spheres,[1,2] emulsions,[3] bioskeletons,[4,5,6] block copolymers,[7,8] surfactants,[9] and small molecules[10] have all been used to induce porosity during the crystallization or precipitation of inorganic materials.

Spontaneous processes that yield porous structures through phase segregation have similarly been developed for a wide range of open-framework inorganic materials. Porous Vycor glass is formed through such a route: a solid precursor segregates into two phases, and the removal of the more soluble phase leaves a porous monolith of the other.[11] Besides spontaneous processes that result in two solid phases, there exist many routes that utilize the controlled segregation of a solid into separate solid and liquid phases[12] or solid and gas phases.[13,14]

Of the many inorganic materials that have been rendered porous, titania is of particular interest because of its high refractive index, large band gap, and the positions of its band edges, which lead to unique optical and electrical properties. TiO_2 nanoparticles have long been used in paints and pigments.[15] Since the classic work of Fujishima and Honda,[16] TiO_2 has been used to photocatalyze the decomposition of small molecules. Most of the work on photoelectrochemical solar cells has made use of colloidal or high surface area TiO_2.[17] Porous titania thin films have been formed through a variety of wet chemical methods, on the basis of metal−organic precursors and block polymers as structure-directing agents.[18,19] Heat treatment of these amorphous titania films leads to the crystallization of nanoparticles of anatase.[20] Macroporous films of titania have been formed through the evaporation and Bénard−Marangoni convection of a titania sol.[21]

* Corresponding author. E-mail: bradc@engineering.ucsb.edu (B.F.C.); seshadri@mrl.ucsb.edu (R.S.).
† Materials Department and Materials Research Laboratory, University of California, Santa Barbara.
‡ Department of Chemical Engineering, University of California, Santa Barbara.

 (1) Holland, B. T.; Blanford, C. F.; Stein, A. *Science* **1998**, *281*, 538.
 (2) Sorensen, E. M.; Barry, S. J.; Jung, H. K.; Rondinelli, J. R.; Vaughey, J. T.; Poeppelmeier, K. R. *Chem. Mater.* **2006**, *18*, 482.
 (3) Imhof, A.; Pine, D. J. *Nature* **1997**, *389*, 948.
 (4) Anderson, M. W.; Holmes, S. M.; Mann, R.; Foran, P.; Cundy, C. S. *J. Nanosci. Nanotechnol.* **2005**, *5*, 92.
 (5) Yang, D.; Qi, L.; Ma, J. *Adv. Mater.* **2002**, *14*, 1543.
 (6) Sieber, H. *Mater. Sci. Eng., A* **2005**, *412*, 43.
 (7) Zhao, D.; Feng, J.; Huo, Q.; Melosh, N.; Fredrickson, G. H.; Chmelka, B. F.; Stucky, G. D. *Science* **1998**, *279*, 548.
 (8) Yang, P.; Zhao, D.; Margolese, D. I.; Chmelka, B. F.; Stucky, G. D. *Nature* **1998**, *396*, 152.
 (9) Beck, J. S.; Vartuli, J. C.; Roth, W. J.; Leonowicz, M.E.; Kresge, C. T.; Schmitt, K. D.; Chu, C. T. W.; Olson, D. H.; Sheppard, E. W.; McCullen, S. B.; Higgins, J. B.; Schlenker, J. L. *J. Am. Chem. Soc.* **1992**, *114*, 10834.
(10) Davis, M. E.; Lobo, R. F. *Chem. Mater.* **1992**, *4*, 756.
(11) Levitz, P.; Ehret, G.; Sinha, S. K.; Drake, J. M. *J. Chem. Phys.* **1991**, *95*, 6151.
(12) Raney, M. US Patent 1.563.787, 1925.
(13) Liu, Y.; Liu, M. *Adv. Eng. Mater.* **2006**, *8*, 89.
(14) Suzuki, Y.; Kondo, N.; Ohji, T. *J. Am. Ceram. Soc.* **2003**, *86*, 1128.
(15) Suyama, Y.; Kato, A. *J. Am. Ceram. Soc.* **1976**, *59*, 146.
(16) Fujishima, A.; Honda, K. *Nature* **1972**, *238*, 37.
(17) O'Regan, B.; Grätzel, M. *Nature* **1991**, *353*, 737.
(18) Crepaldi, E. L.; Soler-Illia, G. J. de A. A.; Grosso, D.; Cagnol, F.; Ribot, F.; Sanchez, C. *J. Am. Chem. Soc.* **2003**, *125*, 9770.
(19) Coakley, K. M.; Liu, Y.; McGehee, M. D.; Frindell, K. L.; Stucky, G. D. *Adv. Funct. Mater.* **2003**, *13*, 301.
(20) Li, D.; Zhou, H.; Honma, I. *Nat. Mater.* **2004**, *3*, 65.
(21) Singh, R. S.; Grimes, C. A.; Dickey, E. C. *Mater. Res. Innovations* **2002**, *4*, 178.

Hierarchically porous structures allow the unusual combination of high material surface area with high diffusivities of guest species. Such properties are useful in applications in which performance depends on the rate of fluid exchange over a surface. Prior work in the preparation of hierarchically porous titania has focused on solution routes involving the condensation of Ti alkoxides. Spontaneous assembly of mesoporous nanoparticles in solution results in macroporous agglomerates with aligned pores.[22] Likewise, surfactant-directed mesostructured titania channels have been formed in macroporous structures arising from sol−gel phase separation in emulsions[23,24] or foams.[25,26]

In our prior work, we have focused on spontaneous phase segregation as a means of inducing porosity in inorganic materials, particularly metals and oxides. These routes have enabled the formation of macroporous binary and ternary oxides, including complex ones, such as the ferromagnetic half-metal $La_{0.7}Sr_{0.3}MnO_3$ and piezoelectric $PbTiO_3$,[27] as well as particles of the Ruddlesden−Popper phase $La_4Ni_3O_{10}$ decorating the walls of a porous NiO monolith.[28] Although the preparation of these materials has relied on the leaching of a sacrificial phase, porosity can also be induced through the leaching of a sacrificial element from within a compound. For example, we have found that placing an oxide containing Zn in a reducing atmosphere at moderate temperature reduces the Zn to its metallic state. Removal of this metallic Zn from the lattice and its subsequent evaporation results in local volume loss that is manifested as porosity.[29,30] Spontaneous structural changes that result in significant volume loss have also proved useful in the formation of mesoporous materials. For example, we have demonstrated that the reduction of Mn_3O_4 results in rocksalt MnO, and the associated volume loss induces mesopores in the resulting structure.[31] We have recently reviewed the uses of such spontaneous methods of pore formation in inorganic materials.[32]

Here, we describe a route to hierarchically porous rutile titania TiO_2, obtained through reduction and vapor-phase leaching of Zn from a macroporous monolith of Zn_2TiO_4 at high temperatures. The resulting highly crystalline rutile TiO_2 has a continuous network of 2−5 μm pores, and the grains that compose the pore walls are themselves porous, with pores sizes ranging from 100 to 200 nm. The transformation from macroporous Zn_2TiO_4 to hierarchically porous TiO_2 was followed by X-ray diffraction and solid-state ^{67}Zn and ^{47,49}Ti

nuclear magnetic resonance (NMR) spectroscopy. Solid-state NMR is sensitive to the local environments around the NMR-active nuclei and therefore yields complementary information to the longer-range structural ordering that is probed by powder X-ray diffraction.

Experimental Section

Powders of anatase TiO_2 (1.598 g, 0.02 mol, mean particle size 50 nm) and wurtzite ZnO (8.13 g, 0.1 mol, mean particle size 500 nm) were mixed thoroughly and pressed into pellets at pressures near 1.6×10^3 kg cm^2. The pellets were subsequently fired in air at 1473 K for 12 h in a covered alumina crucible. To maintain a Zn-rich atmosphere, we also placed powdered ZnO with the pellets in the crucible. The resulting dense monolithic composites of Zn_2-TiO_4 and ZnO were immersed in dilute acid to dissolve the wurtzite ZnO phase. Further leaching of Zn was achieved by placing the resulting macroporous Zn_2TiO_4 monolith in a tube furnace under flowing 5%H_2/N_2, with the temperature ramped at 3 K/min to 1073 K followed by a 4 h soak. A separate set of macroporous Zn_2TiO_4 samples were prepared for X-ray diffraction to monitor the phase evolution during the leaching process. These samples were ramped at 3 K/min under flowing 5%H_2/N_2 to specific temperatures, held for 2 h, and then rapidly cooled to room temperature. X-ray diffraction patterns (XRD) were recorded for all powder samples on a Philips XPERT MPD powder diffractometer in θ−2θ geometry with Cu−Kα radiation (step size, 0.015° in 2θ; step time, 20 s per step). Nitrogen sorption measurements were performed on bulk pellets with a Micrometrics TriStar 3000 instrument at 77 K. Thermogravimetric analysis (TGA) measurements were performed during the vapor-phase leaching process in a 5%H_2/N_2 atmosphere on a Mettler TGA/STGA 851E with a temperature ramp of 1 K/min. Scanning electron microscopy was performed on a FEI XL40 Sirion Microscope.

NMR measurements of both ^{67}Zn ($I = 5/2$, 4.1% natural abundance, sensitivity relative to ^{1}H of 0.0029) and ^{47,49}Ti measurements (^{47}Ti: $I = -5/2$, 7.3% natural abundance, relative sensitivity of 0.0020; ^{49}Ti: $I = -7/2$, 5.5% natural abundance, relative sensitivity of 0.0038) are challenging because of their quadrupolar characters and their low relative sensitivities. Their low gyromagnetic ratios and low natural abundances lead to low signal sensitivities that are exacerbated by resolution challenges arising from the interactions of the ^{67}Zn and ^{47,49}Ti nuclear quadrupole moments with local electric field gradients. In contrast to spin $I = 1/2$ nuclei, such as ^{1}H, ^{13}C, or ^{29}Si, etc., under similar conditions of magic-angle spinning (MAS), quadrupolar interactions are only partially averaged, leading often to significant peak broadening from anisotropic second-order quadrupolar effects. Such second-order quadrupolar interactions scale inversely with the strength of the externally applied magnetic field and are thus mitigated by the use of high magnetic fields. Despite these challenges, ^{67}Zn NMR has been shown to be a powerful probe of local structure in inorganic materials,[33−36] as well as in biochemical systems.[37−39]

The measurement of ^{47,49}Ti NMR spectra is even more challenging. The larger quadrupole moments of both nuclei in com-

(22) Blin, J. L.; Léonard, A.; Yuan, Z. Y.; Gigot, L.; Vantomme, A.; Cheetham, A. K.; Su, B. L. *Angew. Chem., Int. Ed.***2003**, *42*, 2872.

(23) Konishi, J.; Fujita, K.; Nakanishi, K.; Hirao, K. *Chem. Mater.* **2006**, *18*, 864.

(24) Chiu, J.; Bishop, S.; Pine, D J.; Chmelka, B. F. *J. Catal.* **2004**, *221*, 400.

(25) Carn, F.; Achard, M. F.; Babot, O.; Deleuze, H.; Reculusa, S.; Backov, R. *J. Mater. Chem.* **2005**, *15*, 3887.

(26) Maekawa, H.; Esquena, J.; Bishop, S.; Solans, C.; Chmelka, B. F. *Adv. Mater.* **2003**, *15*, 591.

(27) Toberer, E. S.; Weaver, J. W.; Ramesha, K.; Seshadri, R. *Chem. Mater.* **2004**, *16*, 2194.

(28) Toberer, E. S.; Joshi, A.; Seshadri, R. *Chem. Mater.* **2005**, *17*, 2142.

(29) Toberer, E. S.; Seshadri, R. *Adv. Mater.* **2005**, 2244.

(30) Toberer, E. S.; Löfvander, J. P.; Seshadri, R. *Chem. Mater.* **2006**, *18*, 1047.

(31) Toberer, E. S.; Schladt, T. D.; Seshadri, R. *J. Am. Chem. Soc.* **2006**, *128*, 1462.

(32) Toberer, E. S.; Seshadri, R. *J. Chem. Soc., Chem. Commun.* **2006**, 3159.

(33) Dec, S. F.; Davis, M. F.; Maciel, G. E.; Bronniman, C.E.; Fitzgerald, J. J.; Han, S.-S. *Inorg. Chem.* **1993**, *32*, 955.

(34) Wu, G. *Chem. Phys. Lett.* **1998**, *298*, 375.

(35) Barstow, T. J. *Chem. Phys. Lett.* **2003**, *380*, 516.

(36) Zhang, Y.; Mukherjee, S.; Oldfield, E. *J. Am. Chem. Soc.* **2005**, *127*, 2370.

(37) Wu, G. *Biochem. Cell Biol.* **1998**, *76*, 429.

(38) Lipton, A. S.; Heck, R. W.; Ellis, P. D. *J. Am. Chem. Soc.* **2004**, *126*, 4735.

(39) Lipton, A. S.; Wright, T. A.; Bowman, M. K.; Reger, D. L.; Ellis, P. D. *J. Am. Chem. Soc.* **2002**, *124*, 5850.

parison to ^{67}Zn lead, in most cases, to broad resonances that impede the separation of their center-band signals from spinning sidebands under MAS conditions. Static spin−echo measurements are therefore often the most feasible approach for ^{47,49}Ti NMR and have been used here. The measurements are further complicated by the very similar gyromagnetic ratios of the ^{47}Ti and ^{49}Ti nuclei, which lead to resonance frequencies that differ by only 17 kHz, even at a field strength of 19.6 T. Given their broad lines, most ^{47,49}Ti NMR spectra consist of completely overlapping signals from the two isotopes.[40] Because of these challenges, ^{47,49}Ti NMR has received limited attention, though it has been used to characterize local structures in TiO$_2$,[41] metal titanates,[42] titanate perovskites,[43] Ti-containing zeolites,[44] and titania nanoparticles.[45] The availability of higher magnetic fields and improvements in NMR methodology are expected to make ^{47,49}Ti NMR feasible for a wider range of materials in the future.[46,47]

All NMR measurements were performed on a Bruker DRX-830 spectrometer operating at 51.92 MHz for ^{67}Zn and 46.80 MHz for ^{47,49}Ti using a narrow-bore 19.6 T superconducting magnet at the National High Magnetic Field Laboratory in Tallahassee, FL. The NMR experiments were performed at room temperature, using a home-built 4 mm single-resonance probehead with a custom miniature stator made by ICBP, Estonia. To avoid sample distortions from probehead dead times, all spectra were recorded as spin echoes using a standard Hahn−echo pulse sequence. Recycle delays of 1 s were used to allow for relaxation. Solid-state ^{67}Zn MAS NMR spectra were recorded at spinning rates of 10 kHz. ^{67}Zn chemical shifts were referenced to 1.0 M Zn(NO$_3$)$_2$ (0 ppm), and polycrystalline cubic ZnS powder (381 ppm) was used as a secondary reference.[34] Static ^{47,49}Ti chemical shifts were referenced to 1.0 M TiCl$_4$ (0 ppm), and polycrystalline anatase TiO$_2$ powder (−67 ppm) was used as a secondary reference.[45]

Results and Discussion

The reaction between mixed ZnO and TiO$_2$ particles under oxidizing conditions at 1473 K initially yields a dense monolith of mixed ZnO and Zn$_2$TiO$_4$ phases. Figure 1a displays a SEM micrograph of such a dense two-phase monolith. Leaching the ZnO phase in dilute acid renders the pellet macroporous without affecting the micrometer-scale connectivity of the Zn$_2$TiO$_4$ phase. The SEM micrograph in Figure 1b shows that the Zn$_2$TiO$_4$ phase and pore network display high levels of connectivity and that the pores are 2−5 μm in size. The pore volume may be adjusted by changing the initial ratio of ZnO:TiO$_2$. Sintering the monolith in air further improves grain connectivity without significantly disrupting the micrometer-scale pore network, as monitored by scanning electron microscopy. The transformation of macroporous Zn$_2$TiO$_4$ monoliths into hierarchically porous TiO$_2$ is achieved through subsequent reduction and
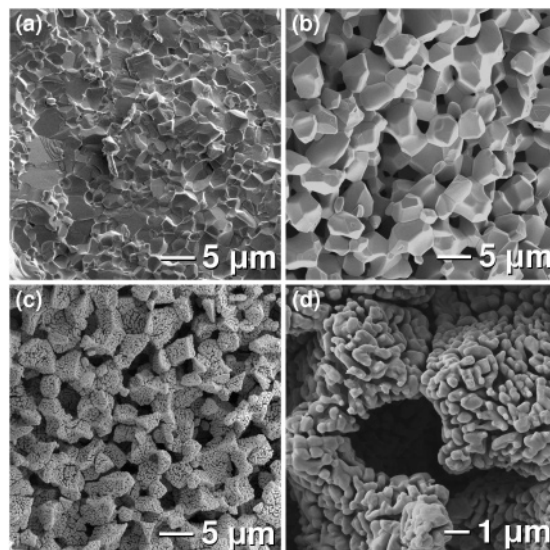
(40) Smith, M. E. *Annu. Rep. NMR Spectrosc.* **2000**, *43*, 121.
(41) Labouriau, A.; Earl, W. L. *Chem. Phys. Lett.* **1997**, *270*, 278.
(42) Padro, D.; Jennings, V.; Smith, M. E.; Hoppe, R.; Thomas, P. A.; Dupree, D. *J. Phys. Chem. B* **2002**, *106*, 13176.
(43) Gervais, C.; Veautier, D.; Smith, M. E.; Babonneau, F.; Belleville, P.; Sanchez, C. *Solid State Nucl. Magn. Reson.* **2004**, *26*, 147.
(44) Ganapathy, S.; Gore, K. U.; Kumar, R.; Amoureux, J.-P. *Solid State Nucl. Magn. Reson.* **2003**, *24*, 184.
(45) Gervais, C.; Smith, M. E.; Pottier, A.; Jolivet, J.-P.; Babonneau, F. *Chem. Mater.* **2001**, *13*, 462.
(46) Bräuniger, T.; Madhu, P. K.; Pampel, A.; Reichert, D. *Solid State Nucl. Magn. Reson.* **2004**, *26*, 114.
(47) Larsen, F. H.; Farnan, I.; Lipton, A. S. *J. Magn. Reson.* **2006**, *178*, 228.

Figure 1. Scanning electron micrographs of (a) a sintered biphasic monolith of ZnO and Zn$_2$TiO$_4$ and (b) the macroporous Zn$_2$TiO$_4$ obtained after leaching of ZnO in alkali. Following transformation to rutile TiO$_2$, the micrometer-scale pores remain as seen in (c), whereas a further level of submicrometer porosity is clearly observed at higher magnification in (d).
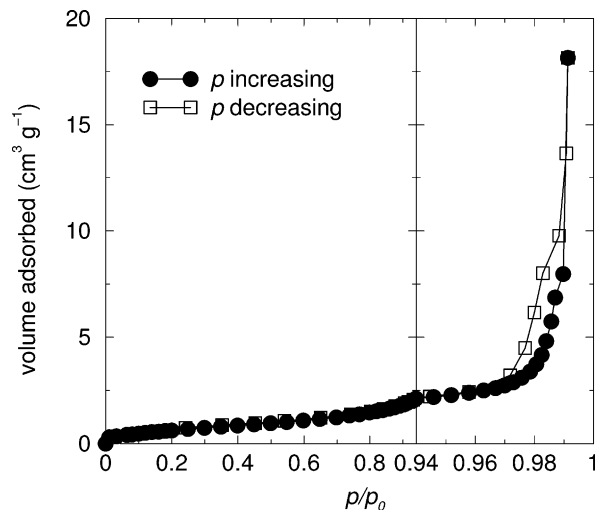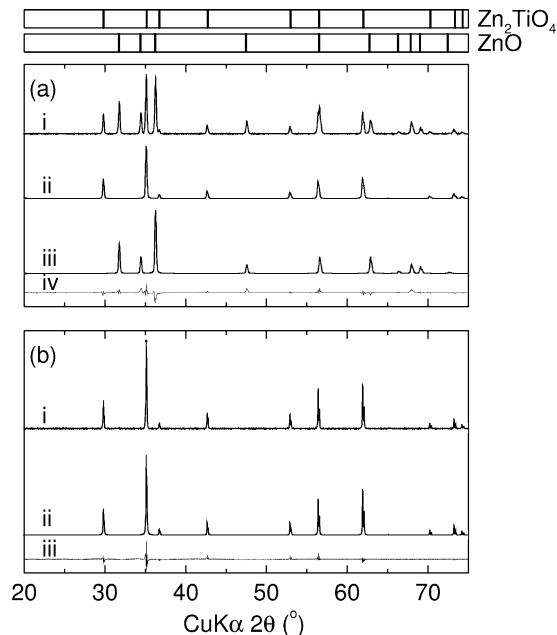

Figure 2. N$_2$ sorption isotherm for hierarchically porous TiO$_2$ prepared as described in the text. Hysteresis is observed only at high pressures, indicative of the filling of micrometer-size pores.

vapor-phase leaching of Zn in flowing 5%H$_2$/N$_2$. Under these conditions, Zn is reduced to its elemental state, volatilized, and transported downstream out of the hot zone of the furnace. Zinc reduction correspondingly results in the formation of water, which is similarly transported downstream. Monoliths of TiO$_2$ thus formed maintain their original macropore morphologies (Figure 1c) and additionally develop submicrometer (100−200 nm) porosity in the macropore walls (Figure 1d).

Evidence for hierarchical porosity in the final TiO$_2$ product is obtained from N$_2$ sorption measurements (Figure 2), which yielded a surface area of 5 m^2 g^{-1}. Such a value is typical for materials with pores sizes in the tens of nanometers observed in SEM images.[29] For example, a monolith of titania perforated with 150 nm pores and a total volume porosity of 50% should, from its known density, possess a surface area of 6 m^2 g^{-1}. From Figure 2, we observe hysteretic behavior of the sorption at $p/p_0 > 0.95$, which is indicative

Figure 3. Powder XRD data and Rietveld refinement of (a) the biphasic Zn_2TiO_4/ZnO composite, showing (i) the experimental diffraction pattern, (ii) a fit to the spinel structure of Zn_2TiO_4, (iii) a fit to the wurtzite structure of ZnO, and (iv) the difference profile. Relative mole ratio of 2.9:1 ZnO: Zn_2TiO_4 was obtained from the refinement. (b) After leaching in alkali, no detectable ZnO remains and the sample is pure Zn_2TiO_4: (i) the experimental diffraction pattern, (ii) a fit to the spinel structure of Zn_2TiO_4, and (iii) the difference profile. Vertical lines at the top of the figure indicate expected peak positions for the spinel Zn_2TiO_4 and wurtzite ZnO phases.

of the filling of large (>50 nm) pores.[48] We have explored control of pore size in the two different levels of hierarchy in this and other systems.[30] The macroporous network is obtained through leaching of one phase from a two-phase composite. In principle, the relative amounts of the two phases in the composite and the manner in which they are prepared should permit control of macropore size. However, in practice, we find that preparation conditions that yield robust macroporous materials have until now been associated with pores in the micrometer size range. Similarly, for the case of the smaller pores, when the crystallites making up the macroporous material are subject to leaching (here, of Zn and O removed in the vapor phase), the complete removal of Zn requires conditions wherein some coarsening of the pores take place. Although structures as small as 10 nm are observed initially, final average pore sizes are frequently in the 50−100 nm range.

To understand the evolution of the mixed inorganic phases during the preparation and the subsequent leaching of the zinc titanate monoliths, we obtained powder X-ray diffraction patterns after each step and analyzed them using the Rietveld technique implemented in the XND code.[49] As shown in Figure 3a, the dense two-phase composite whose SEM image is shown in Figure 1a was found, as expected, to be a mixture of wurtzite ZnO ($P6_3mc$) and cubic Zn_2TiO_4 ($Fd\bar{3}m$). Quantitative phase analysis using Rietveld scale factors yielded an estimated ZnO:Zn_2TiO_4 mole ratio of 2.9:1, which

(48) Brunauer, S. *The Adsorption of Gases andVapors*; Princeton University Press: Princeton, NJ, 1943; Vol. I, Physical Adsorption.
(49) Bérar, J.-F.; Garnier, P. *NIST Special Publication* **1992**, *846*, 212; freely available from the CCP14 Web site at http://www.ccp14.ac.uk.
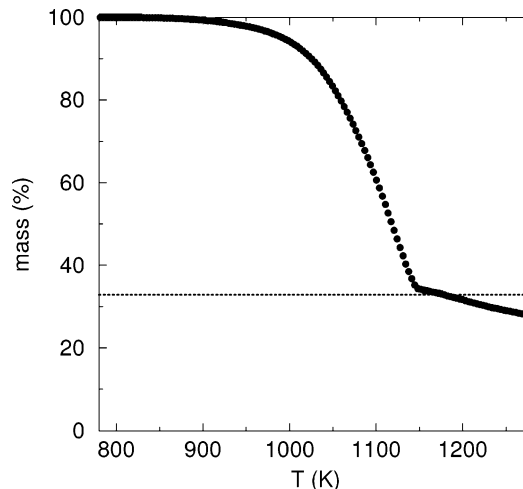

Figure 4. Thermogravimetric analysis of Zn_2TiO_4 in a 5% H_2/N_2 atmosphere, heated at a rate of 1 K/min. Mass loss due to Zn reduction and volatilization begins by 900 K and is finished by 1150 K. The dotted horizontal line represents the expected mass loss for the conversion of Zn_2- TiO_4 to TiO_2. Further mass loss is due to partial reduction of TiO_2 and the associated oxygen loss.

is in close agreement with the value of 3:1 expected for the ratio of starting materials used. Figure 3b shows the XRD pattern after acid leaching of the ZnO phase. Rietveld refinement confirms phase-pure Zn_2TiO_4, within the limits of detectability. A mass loss of 52.7% was measured as a consequence of the leaching, in close agreement with the expected value of 52.4% suggested by XRD. From the mass loss and knowing the bulk densities of the two phases, a greater than 50% volume porosity is inferred for the macroporous Zn_2TiO_4. The low solubility of Ti in ZnO and minimal Zn loss during the initial high-temperature oxidation account for the excellent agreement between the expected and measured values.

The transformation of macroporous Zn_2TiO_4 into TiO_2 was monitored by thermogravimetric analysis in a 5% H_2/N_2 reducing atmosphere. From Figure 4, we observe that the reduction of Zn_2TiO_4 begins near 900 K, and by 1150 K, the mass loss agrees with complete conversion to TiO_2 (67% mass loss). We attribute the continued decrease in mass above 1150 K to oxygen loss from the final titania product. The evolution of phases during the mass loss has been followed by X-ray diffraction acquired after reduction/ leaching of Zn_2TiO_4 at several intermediate temperatures from 925 to 1025 K. Figure 5 displays powder XRD patterns for isothermal reductions performed for 2 h at the indicated temperatures. Data acquired after 12 h reduction at 1025 K are also shown. At 925 K, the XRD pattern continues to indicate phase-pure Zn_2TiO_4, despite a 12% mass loss, and the material acquire a dark blue-gray color. By 975 K, a significant amount of Zn has been reduced and volatilized, along with its corresponding oxygen ion, leaving behind a mixture of Zn_2TiO_4 and $Zn_2Ti_3O_8$, as evident from their respective XRD reflections. The intermediate $Zn_2Ti_3O_8$ phase is a defect spinel $Zn[Ti_{1.5}\square_{0.5}]O_4$, which is a metastable structure in the space group $P4_322$.[50] Reflections from TiO_2 polymorphs (anatase and rutile) are detected following 2 h

(50) Steinike, U.; Wallis, B. *Cryst. Res. Technol.* **1997**, *32*, 187.

◇ TiO_2 rutile
+ TiO_2 anatase
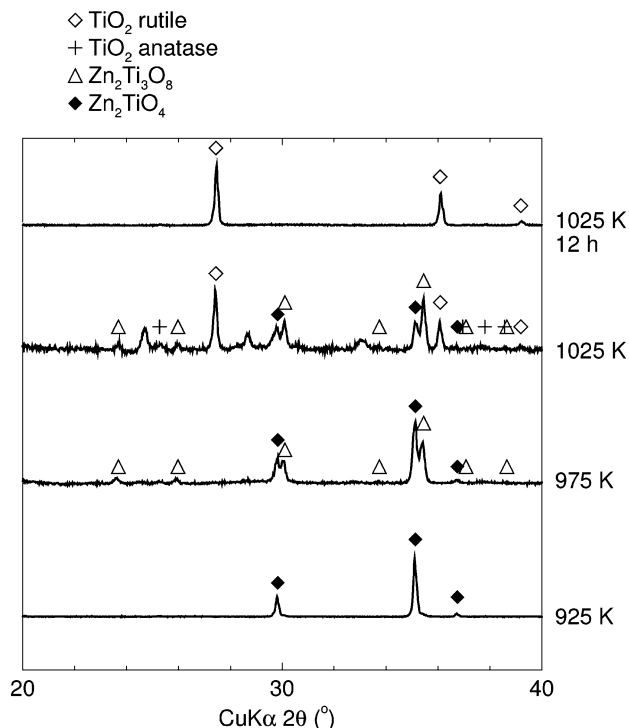△ $Zn_2Ti_3O_8$
◆ Zn_2TiO_4

Figure 5. Powder XRD data showing the evolution of Zn_2TiO_4 and its products after vapor-phase leaching of Zn as a result of heating in a reducing atmosphere (5%H_2/N_2) for 2 h intervals. Zn_2TiO_4 begins to transform to the intermediate phase $Zn_2Ti_3O_8$ by 975 K, as Zn^{2+} is reduced and volatilized. By 1025 K, polymorphs of TiO_2 begin to appear and the material becomes phase-pure rutile TiO_2 after 12 h at this temperature.

reduction at 1025 K, and after 12 h at this temperature, rutile TiO_2 is the only phase present. The presence of multiple polymorphs of nanostructured titania is common because of competition between surface and volume free energies.[51] Additional unlabeled low-angle peaks are found (not shown here) that are attributed to shear phases of slightly reduced titania.[52]

The morphologies of the samples during the different stages of the transformation from Zn_2TiO_4 to TiO_2 were examined by scanning electron microscopy. Figure 6 shows SEM images for the same samples as studied in Figure 5, subjected to varying reduction treatments. The micrographs show that the initial stages of leaching of Zn and O from Zn_2TiO_4 result in aligned dendritic TiO_2 structures that penetrate the sample, with the most dense regions being buried within. They also demonstrate that the shapes and cross-sections of the dendrites can be modified depending on the reducing conditions. Grains of a sample partially leached at 923 K for 12 h are shown in Figure 6a−c. Figure 6a shows two grains coated with TiO_2 dendrites, and in 6b, the dendrites have been broken to reveal the dense underlying spinel. A cross-section through the grains reveals the columnar morphology of the TiO_2 (Figure 6c). Such aligned dendrites are observed under other leaching conditions, as shown in Figure 6d for a sample leached at 973 K for 8 h. Images e and f of Figure 6 show that with increasing
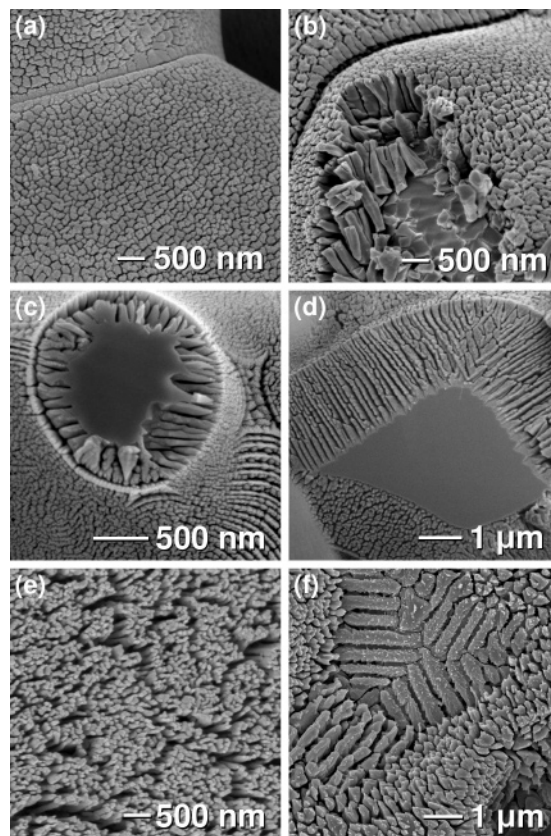
(51) Ranade, M. R.; Navrotsky, A.; Zhang, H. Z.; Banfield, J. F.; Elder, S. H.; Zaban, A.; Borse, P. H.; Kulkarni, S. K.; Doran, G. S.; Whitfield, H. J. *Proc. Natl. Acad. Sci. U.S.A.* **2002**, *99*, 6476−6481.
(52) Hyde, B. G.; Andersson, S. *Inorganic Crystal Structures*; John Wiley and Sons: New York, 1989.
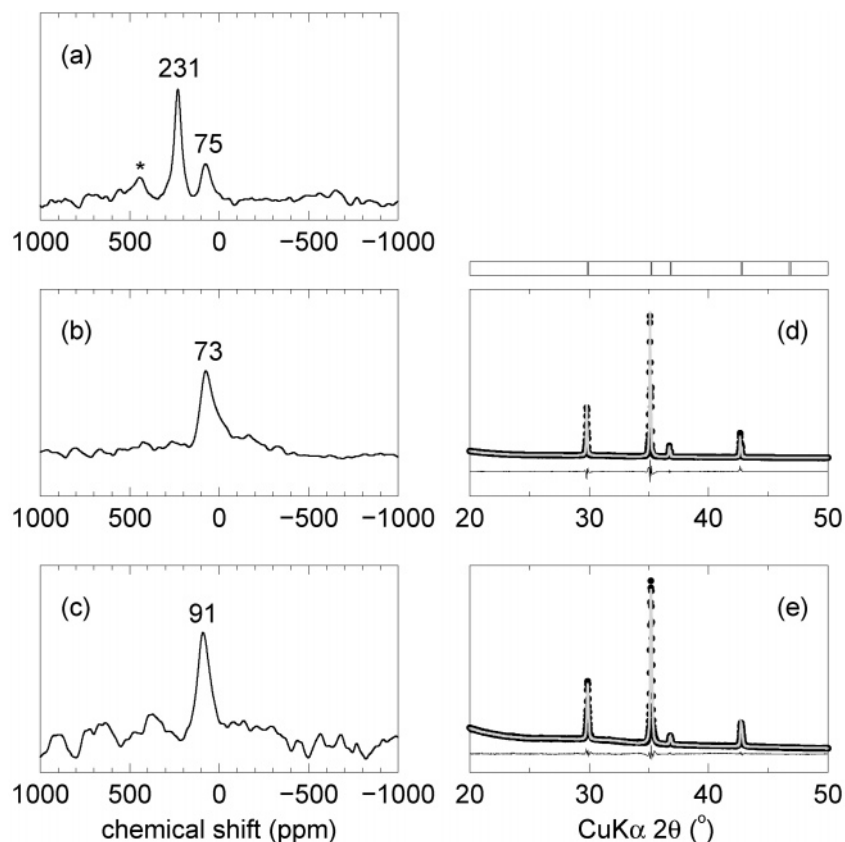

Figure 6. SEM images of partially reduced macroporous Zn_2TiO_4 showing the development of porosity after various extents of reduction and vapor-phase leaching: (a) Two grains of macroporous Zn_2TiO_4 after brief reduction at 923 K for 12 h. (b) The same sample showing that reduction/leaching leads to the formation of TiO_2 in the form of dendrites, some of which were broken to reveal the underlying dense Zn−Ti−O inverse spinel. (c) A cross-sectional view of the same sample as in (a) and (b) showing a fracture surface across a macropore wall. The dense material in the middle is again the inverse spinel. (d) A sample prepared at 973 K for 8 h, showing aligned TiO_2 dendrites that are representative structural features. (e) and (f) are top-down views of nanorods and laths of TiO_2 obtained after reduction/leaching at 998 K for 12 h and (f) at 1023 K for 4 h, respectively.

temperature, the formation of aligned rods is preserved and the rod diameter begins to increase. Figure 6e shows that TiO_2 rods formed at 998 K for 12 h and Figure 6f shows that similar structures formed at 1023 K for 4 h.

Such hierarchical porosity is similar to that observed for manganese oxide MnO prepared by vapor-phase leaching of Zn and O from a $ZnMn_2O_4$ precursor.[29,30] In that case, the reduction of $ZnMn_2O_4$ to rocksalt $Zn_{0.33}Mn_{0.67}O$ induced the formation of mesopores in the rocksalt grains (at 725 K). Further reduction and leaching of Zn from the rocksalt lattice (at 925 K) additionally increased the mesopore volume, leading to a crystalline MnO structure with greater than 80% total porosity.

In both $ZnMn_2O_4$ and Zn_2TiO_4, porosity arises that is due to volume loss. However, the precise pathways for such volume loss in these two materials are quite different. In the manganese-based spinels, Mn^{3+} is reduced to Mn^{2+} with a corresponding change from the spinel to the rocksalt structure. In Zn_2TiO_4, pores are again formed that are due to volume loss associated with the Zn_2TiO_4-to-$Zn_2Ti_3O_8$ conversion. Significant restructuring is required to transform the inverse spinel $Zn[TiZn]O_4$ to the defect spinel $Zn[Ti_{1.5}\square_{0.5}]O_4$, which requires the loss of Zn and an O counterion from

Figure 7. Spin−echo [67]Zn MAS NMR spectra acquired at 19.6 T, a spinning rate of 10 kHz, and room temperature for powder samples of: (a) dense biphasic ZnO and Zn_2TiO_4; (b) the product after acid-leaching to form macroporous Zn_2TiO_4; and (c) after subsequent partial reduction in 5%H_2/N_2 at 1023 K for 1 h. The somewhat higher noise level in Figure 7c arises from the lower Zn content and a smaller amount of sample measured. The important shifts, in parts per million, are indicated above each peak and the asterisk marks a spinning sideband. (d) and (e) show the powder X-ray diffraction data and Rietveld refinements for macroporous Zn_2TiO_4, alongside their corresponding [67]Zn MAS spectra.

the spinel, as well as a relative increase in the number of Ti atoms per unit cell. This suggests that the transformation is not simply due to a gradual decrease in the Zn:Ti ratio following Zn volatilization but involves significant diffusion of Ti ions as well. The aligned pore structures observed for the partially transformed samples shown in the different panels of Figure 6 suggest this phase change occurs topotactically. The different pathways by which phases develop and evolve in the manganese and Ti systems are also manifested in their respective thermogravimetric traces. Although a two-step mass loss was observed for $ZnMn_2O_4$ (at temperatures of 670 and 850 K), Zn_2TiO_4 displays a single large mass loss, which occurs at a higher temperature (1000 K).

Solid-state [67]Zn magic-angle-spinning NMR measurements were performed at 19.6 T and a 10 kHz spinning rate to follow the structural changes in the local environments of [67]Zn nuclei. At this very high magnetic field strength (830 MHz for ^{1}H), both the sensitivity and resolution of the low natural abundance (4.1%), low gyromagnetic ratio, and quadrupolar ($I = 5/2$) [67]Zn nuclei are crucially improved. This allows clear differences in the local [67]Zn environments to be observed, as the starting 3:1 ZnO:Zn_2TiO_4 material is converted into macroporous Zn_2TiO_4. Figure 7a shows the spin−echo [67]Zn MAS spectrum of the 3:1 ZnO:Zn_2TiO_4 starting material, which yields at least two well-resolved peaks at 231 ppm (50 ppm, full width at half-maximum (fwhm)) and 75 ppm (60 ppm fwhm), corresponding to ZnO

and Zn_2TiO_4, respectively. The integrated areas of the two peaks and spinning sidebands are approximately consistent with their relative Zn stoichiometries and mole ratios. By comparison, [67]Zn MAS experiments (not shown here) of bulk polycrystalline ZnO powder performed under the same conditions yielded a single resonance at 232 ppm (30 ppm fwhm) and those of pure bulk polycrystalline Zn_2TiO_4 yielded a single resonance at 65 ppm (55 ppm fwhm). The spin−echo [67]Zn MAS spectrum in Figure 7b of the same material in Figure 7a after acid leaching also shows only one resonance at 73 ppm (70 ppm fwhm), corresponding to the remaining $ZnTi_2O_4$ phase, which is not significantly affected by the leaching process. The absence of a [67]Zn signal near 230 ppm indicates that the ZnO phase has been completely removed (within the limits of detectability). This removal of ZnO is in agreement with the XRD data presented in Figure 3.

Local Zn environments can similarly be characterized and their changes monitored during reductive leaching of Zn from Zn_2TiO_4 to form hierarchically porous TiO_2. For example, at an intermediate stage of reduction (9% mass loss and a color change from white to dark blue after 1 h at 1023 K under 5%H_2N_2), the [67]Zn MAS spectrum shows a single resonance at 91 ppm (60 ppm fwhm) (Figure 7c). These changes are attributed to changes in the oxidation state of nearby Ti species. Interestingly, little broadening of the [67]Zn resonance is observed, indicating that the Zn environments are relatively uniform at the level of near neighbors at this
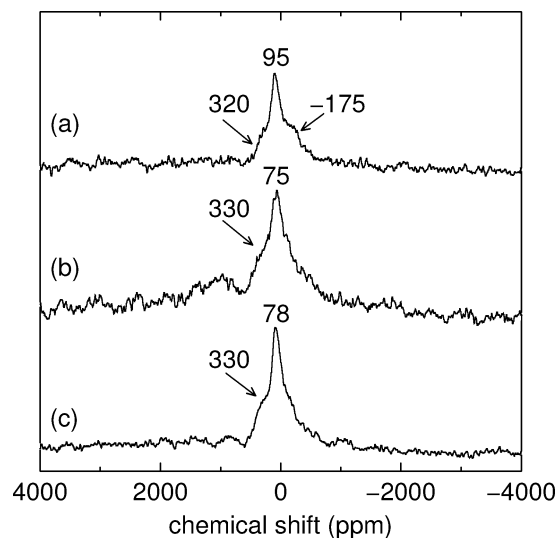
Figure 8. Static spin−echo ^{47,49}Ti NMR spectra acquired at 19.6 T and room temperature of (a) macroporous Zn_2TiO_4 after acid leaching and (b, c) of the same sample after subsequent reduction in flowing 5%H_2/N_2 at 1023 K for (b) 1 and (c) 12 h. Prominent shifts and shoulder features are indicated in ppm.

stage of reduction. It is possible that the ^{67}Zn shift responds to changes in the environment caused by reduction of some of the Ti^{4+} to Ti^{3+}. The XRD patterns in parts d and e of Figure 7 are nearly identical, indicating almost no differences in the crystallinities of the macroporous zinc titanate before and after partial reduction, apart from a small contraction in the inverse spinel cell parameter from 8.4711(2) to 8.4616-(4) Å. Such a contraction is consistent with the trend in unit-cell parameter expected for a transition from the inverse spinel Zn_2TiO_4 to the defect spinel $Zn[Ti_{1.5}\square_{0.5}]O_4$, which has a cell parameter of 8.392 Å.[50]

Changes in the local chemical and electronic environments of Ti species during the reduction of Zn_2TiO_4 to hierarchically porous TiO_2 could be followed by static ^{47,49}Ti NMR measurements. Figure 8a shows the static ^{47,49}Ti NMR spectrum of macroporous Zn_2TiO_4, which yields a broad signal with a dominant resonance at 95 ppm and pronounced shoulders at −175 and 320 ppm. Upon reduction of the sample after 1 h in 5%H_2/N_2 at 1023 K, clear changes in the ^{47,49}Ti spectra suggest changes in the local environment of the titania moieties present. As shown in Figure 8b, the ^{47,49}Ti resonance at −175 ppm diminishes in relative intensity, whereas the shoulder at ≈330 ppm becomes more pronounced. After more complete reduction (12 h under identical conditions), it is seen in Figure 8c that the downfield shoulder at 330 ppm becomes more prominent, reflecting decreased electronic shielding of these ^{47,49}Ti species in the sample. Such deshielding is consistent with the occupation of empty Ti 3d and 4s orbitals associated with the reduction

of Ti^{4+} to Ti^{3+}, which is also evidenced by a change in the sample color from white to dark blue. The line shapes of the ^{47,49}Ti NMR signals in all of the samples reflect multiple overlapping ^{47}Ti and ^{49}Ti powder patterns that are broadened by anisotropic interactions and contributions from multiple Ti chemical or electronic environments in the samples. Such complexity precludes, for the spectra displayed here, unique deconvolution of the signal(s) into contributions from individual powder patterns.

In summary, the rich chemistry and structures that underlie the Zn−Ti−O phase diagram, including especially the two-phase regions, can be exploited to prepare a wide range of porous inorganic solids with unusual micrometer- and submicrometer-scale porous structures. Moreover, as a consequence of the high processing temperatures used, the resulting porous materials are highly crystalline, as shown specifically for the stable and technologically important rutile polymorph of titania. Such materials can furthermore be prepared with porosity on multiple length scales, often with aligned rodlike or lathlike nanostructural features. Direct insights on the local environments of Zn and Ti species in these structures, as well as their respective transformations during processing, are provided by high-field ^{67}Zn and ^{47,49}Ti MAS NMR, which correlate well with electron microscopy, X-ray diffraction, sorption, and thermogravimetric analyses. The phase partitioning, reactions, and nanostructuring that take place are spontaneous and thermodynamically favorable under the given conditions of temperature and gas atmosphere. The use of solid−gas and solid−solid reactions allows highly stable crystalline inorganic materials with hierarchically porous architectures to be formed without the need for other structure-directing agents. Such an approach provides new means for controlling multiscale material composition, structure, and porosity, especially those that require high processing temperatures.